Chapter

Reconfigurable Fabry-Pérot Cavity Antenna Basing on Phase Controllable Metasurfaces

Peng Xie, Guangming Wang, Haipeng Li, Yawei Wang and Xiangjun Gao

Abstract

Fabry-Pérot cavity (FPC) antenna is a kind of high-gain antenna. Compared with other high-gain antennas, such as array antenna and reflector antenna, the FPC antenna enjoys the advantages of simple structure and high efficiency. So it has attracts many attention since proposed. However, it also suffers the disadvantages of narrow band and fixed radiation patterns, due to its resonance structure. In order to overcome these disadvantages, we proposed novel strategies to realize reconfigurable FPC antennas using the phase controllable metasurfaces (MSs). Through adding PIN diodes into every unit cell of the MS, the reflection phase of the MS can be controlled by tuning the states of the diodes. Then the designed phase controllable MSs are used as the partially reflection surfaces (PRS) to realize frequency or radiation pattern reconfigurable FPC antennas. In this chapter, we analyze the basic theory of the FPC antenna and describe its radiation principle firstly. Then, reflection phase controllable MSs are designed and applied to the FPC antennas. Thus frequency and radiation pattern reconfigurable FPC antennas are formed. The design processes are described in details, and the proposed antennas are fabricated and measured. The measured results verify the correctness of the designs. Through this chapter, the readers can form a comprehensive understanding of reconfigurable FPC antenna design.

Keywords: metasurface, Fabry-Pérot cavity, reconfigurable, phase controllable, PIN diode

1. Introduction

The leaky-wave antennas have attracted much attention since proposed and found wide applications in wireless communication systems. As one kind of the leaky-wave antenna, Fabry-Pérot cavity (FPC) antennas are preferred by scientists due to their broadside pattern and high-gain performance. However, the FPC antenna usually suffer some disadvantages due to its inherent limitations of the resonate structure, such as narrow band, fixing beam, and high profile. So many researches have been done on wideband and beam tilted FPC antenna. To overcome these disadvantages of the conventional FPC antenna, we proposed novel strategies that realize reconfigurable FPC antennas using the PIN diodes. In this chapter, we designed three reconfigurable FPC antennas by metasurfaces (MSs).

Through adding PIN diodes on the MS, the reflection phase of the MS can be controlled by tuning the states of the diodes. The different reflect phase distributions of the MS can make the FPC antenna present different frequency and radiation performance. The reconfigurable FPC antenna can improve the performance of antenna, so that the antenna can be widely used.

2. Basic theory of the Fabry-Pérot cavity antenna

Due to its well frequency selection characteristics, the Fabry-Pérot (FP) resonate cavity are widely used in many applications, such as spectral analyzer, interference filter, and so on. The FP resonate cavity can also be used in the design of high-gain antennas [1–4]. Adding a feeder into the cavity, the electromagnetic wave emanating from the feeder experiences multiple reflections and transmissions in the cavity [5, 6]. When the resonance condition is satisfied, the wave coming out of the cavity will be in phase, and then bidirectional high-gain radiation is achieved. However, most applications require unidirectional antenna radiation. So the FP resonate cavity should be changed slightly to design high-gain FPC antenna [7–9].

In practice, the artificial partially reflection surfaces (PRS) are usually used to design FPC antenna. In order to realize unidirectional radiation, one of the PRS of the FP resonate cavity should be replaced by the metal ground plane [10–12]. The PRS and the metal ground plane form the resonate cavity of the FPC antenna. The schematic model of the FPC antenna is shown in **Figure 1**. The distance between the PRS and the ground plane is h. The radiator locates in the middle of the cavity above the ground plane. The electromagnetic wave emanating from the radiator is incident on the PRS with an angle of θ. One part of the electromagnetic wave transmits through the PRS and the other part is reflected into the cavity by the PRS. The reflected wave is totally reflected by the ground plane and is incident to the PRS again with the same angle, forming the secondary transmission and reflection. The electromagnetic wave experiences multiple reflections and transmissions between the PRS and the ground plane and finally all get through the PRS [11, 13, 14].

Assuming that the transmission coefficient and reflection coefficient of the PRS are

$$r = Re^{j\varphi_1}, \quad t = Te^{j\theta_1} \tag{1}$$

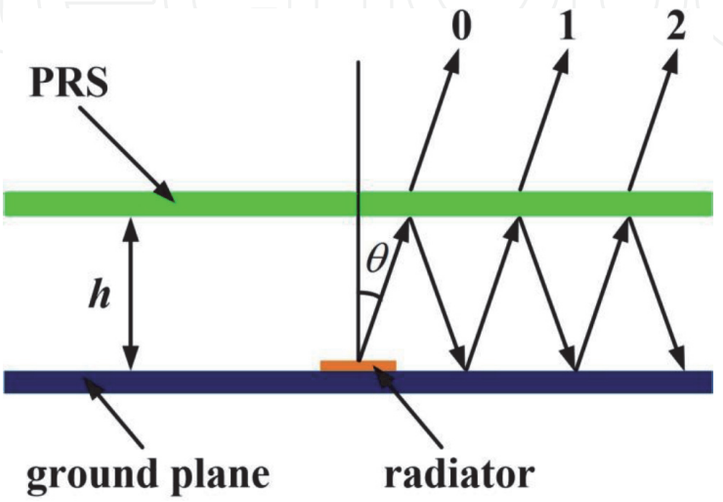

Figure 1.
The schematic model of the FPC antenna.

then the first transmission coefficient is

$$t_0 = t \tag{2}$$

After once reflected by the PRS, the transmission coefficient is

$$t_1 = tre^{-2jkh/\cos\theta + 2jkh\tan\theta\sin\theta + j\varphi_2} = tre^{-2jkh\cos\theta + j\varphi_2} \tag{3}$$

where φ_2 is the reflection phase of the metal ground plane, λ is the wavelength in the free space, and $K = 2\pi/\lambda$ is the propagation constant. According to the above equation, it can be deduced that the transmission coefficient of the resonate cavity after n times of reflection is

$$t_n = tr^n e^{-2jnkh\cos\theta + in\varphi_2} \tag{4}$$

So, the total transmission coefficient along θ direction is

$$t_{total} = \sum_{n=0}^{\infty} t_n = t\sum_{n=0}^{\infty} r^n e^{-2jnkh\cos\theta + jn\varphi_2} = \frac{t}{1 - re^{-2jkh\cos\theta + j\varphi_2}} \tag{5}$$

According to the energy conservation law, $T^2 = 1 - R^2$. Therefore, the total power transmission coefficient is

$$D = t_{total}t_{total}^* = \frac{1 - R^2}{1 + R^2 - 2R\cos\Phi} \tag{6}$$

where

$$\Phi = \frac{4\pi}{\lambda}h\cos\theta - \varphi_1 - \varphi_2 \tag{7}$$

φ_1 is the reflection phase of the PRS. According to Eq. (6), when $\cos\Phi = 1$, the maximum value of the power transmission coefficient is

$$D = \frac{1 - R^2}{1 + R^2 - 2R} = \frac{1 + R}{1 - R} \tag{8}$$

It can be seen that the power transmission coefficient is mainly relative to the reflection magnitude of the PRS. The power transmission coefficient increases with the increase of the reflection magnitude of the PRS, so does the gain of the antenna. The maximum radiation direction of the antenna is $\theta = 0°$. And the resonate condition of the antenna is

$$h = \frac{\lambda}{4\pi}(\varphi_1 + \varphi_2) + \frac{\lambda}{2}N, \quad N = 0, 1, 2\ldots \tag{9}$$

3. Frequency reconfigurable Fabry-Pérot antenna

3.1 Design of the reconfigurable PRS

In order to realize the reflection phase configuration of the PRS, the unit cell of the PRS must be configurable [15]. The structure of the unit cell is shown in **Figure 2a**. The unit cell is printed on a substrate of FR4 with a thickness of 1.6 mm and

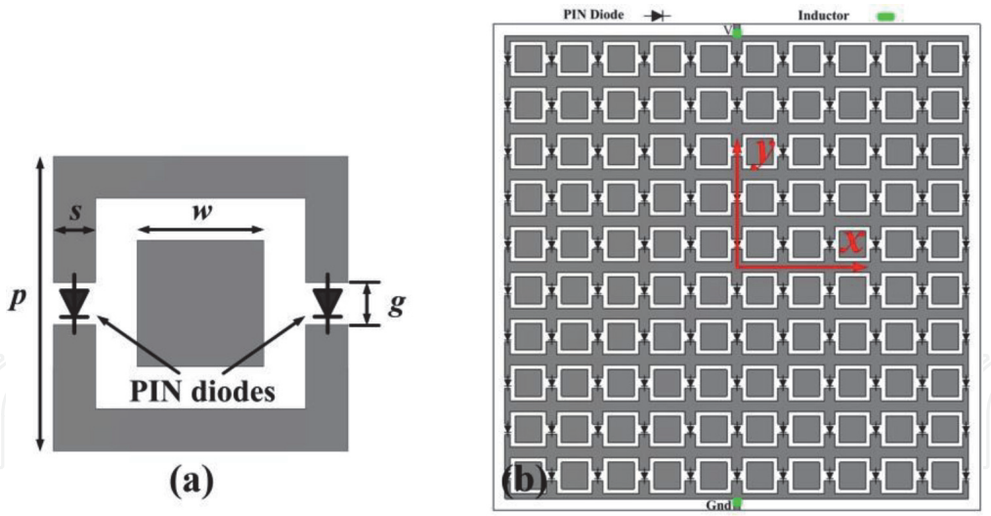

Figure 2.
(a) The structure of the unit cell and (b) the view of reconfigurable PRS.

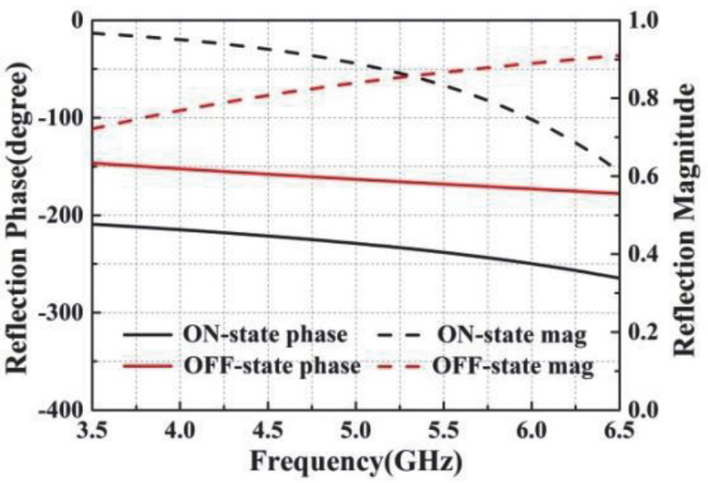

Figure 3.
Reflection coefficients of the unit cell.

permittivity of 4.4. It consists of a square patch and a square ring. Two slots are added on the square ring, and two PIN diodes are inserted into the slots. The two PIN diodes are controlled simultaneously. When diodes are in different states, the unit cell presents different reflection phases. **Figure 3** shows the simulation reflection coefficients of the unit cell with w = 7 mm. We can see that, when the diode state changes from OFF to ON, the reflection phase of the unit cell is delayed. According to Eq. (9), the λ increases with the decrease of φ_1. So the antenna will operate at low frequency when the diodes are ON and high frequency when the diodes are OFF. Besides, the reflection phase of the unit cell with the variation of w is plotted in **Figure 4**. It can be seen that the reflection phase of the unit cell decreases with the increase of w no matter if the diodes are open or closed. So the w can be used in tuning the reflection phase of the unit cell to meet the requirement of the antenna.

Figure 2b shows the structure of the configurable PRS. It consists of 10 × 10 unit cells. All diodes on the PRS are set along the same orientation, so all diodes can be controlled by only one DC source. The biasing point V on the top of the PRS connects the anode of the DC source, and the biasing point Gnd on the bottom of the PRS connects the cathode of the DC source. Inductors are added between the feeding point and the metal structure on the PRS to prevent the RF signal from entering the DC source. The periodic boundary is adopted in the simulation of the unit cell, so the

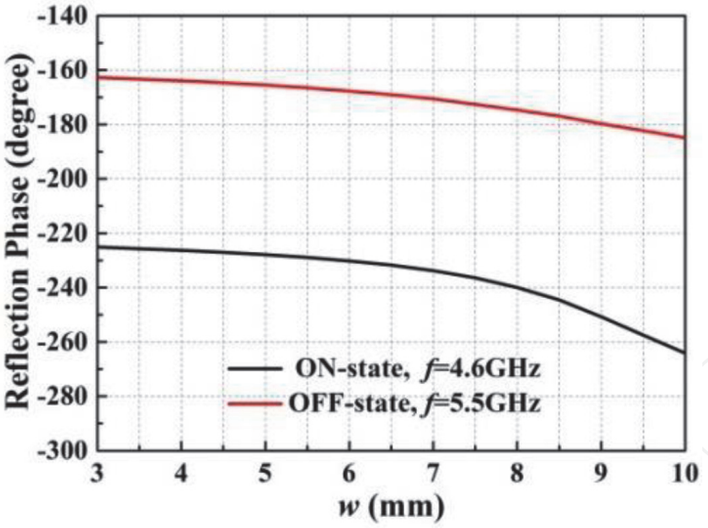

Figure 4.
Effect of w *on reflection phase of the unit cell.*

reflection phase of the unit cell can be considered as the reflection phase of the PRS. The diodes are the BAR50-03 W from Infineon. Because there is no model of the diode in the CST, it is replaced by the equivalent circuit in the simulation. When the diode is closed, they can be replaced by resistors of 1 Ω. When the diode is open, it is replaced by a circuit that consists of a 10 kΩ resistor in parallel with a 0.15 pF capacitor.

3.2 Antenna design

In order to realize frequency reconfiguration, the FPC antenna must adopt dual-band feeder. So we design a dual-band microwave antenna as the feeder of the FPC antenna. The structure of the feeder antenna is shown in **Figure 5a**. The antenna is printed on a substrate of FR4 with the permittivity of 4.4 and thickness of 1.6 mm. It consists of two different metal patches which are connected by a microwave line. Two patches have different lengths and widths, so they can resonate at different frequencies. The bottom of the substrate is a metal ground plane. A SMA connecter is used to feed the antenna from the bottom side, and the feeding point is on the microstrip line. The antenna can realize impedance matching through tuning the position of the feeding point and the microstrip line. The feed antenna is designed to work at 4.6 and 5.5 GHz.

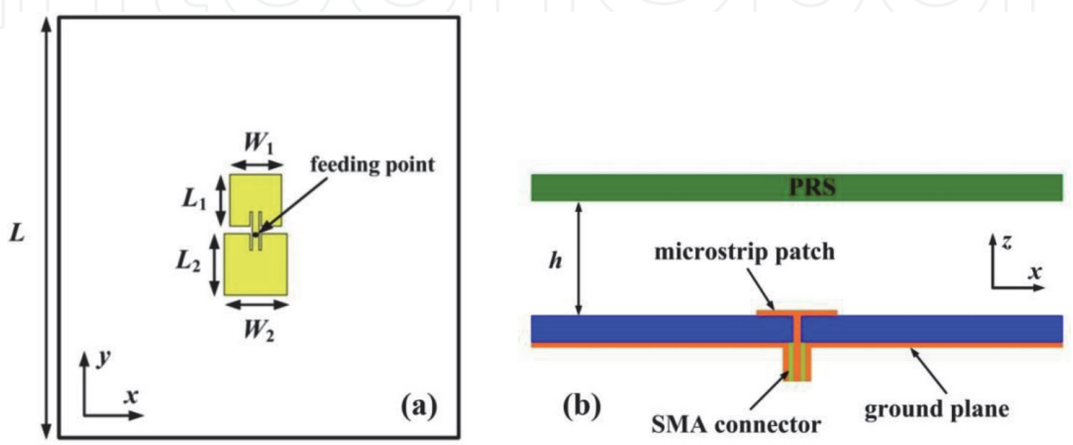

Figure 5.
Reflection coefficients of the unit cell. Geometry of the antenna: (a) top view of the feed antenna and (b) side view of the FPC antenna.

Next, we will introduce how to realize the dual-band working of the antenna through tuning the reflection phase of the PRS. **Figure 5b** shows the geometry of the FPC antenna. We consume that the height of the cavity is h_L when the antenna work at low frequency and h_H when the antenna work at high frequency. According Eq. (9), they can be expressed as.

$$h_L = \frac{(\varphi_L + \varphi_2)\lambda_L}{4\pi} + \frac{N_L\lambda_L}{2} \tag{10}$$

$$h_H = \frac{(\varphi_H + \varphi_2)\lambda_H}{4\pi} + \frac{N_H\lambda_H}{2} \tag{11}$$

When $h_L = h_H$, it can be considered as the antenna operates at two different frequencies without changing the antenna structure. In Eqs. (10) and (11), the N is set to 1 to obtain low profile of the antenna. The antenna is designed to work at 4.6 and 5.5 GHz, so λ_L = 65.2 mm and λ_H = 54.5 mm. The reflection phase of the metal ground plane φ_2 is always π; thus the h is only related to the reflection phase of the PRS. The φ is related to the width of the patch in the unit cell. So we can deduce the relationship between h and w, as shown in **Figure 6**. The black line is the relationship

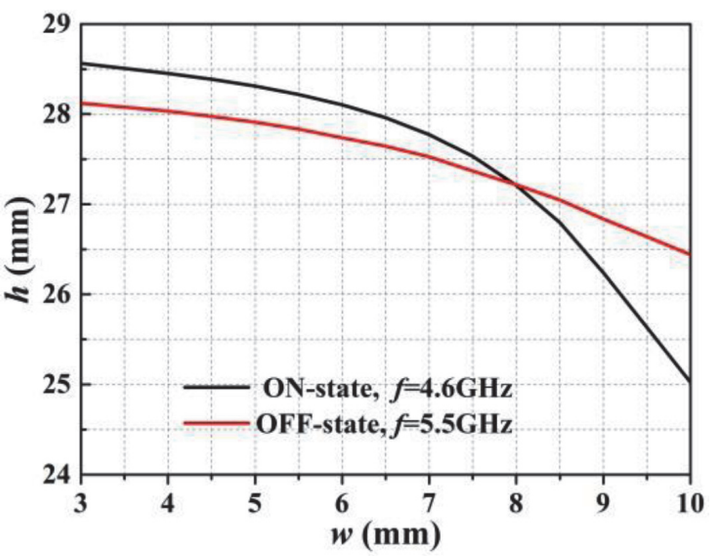

Figure 6.
The relationship between w *and* h.

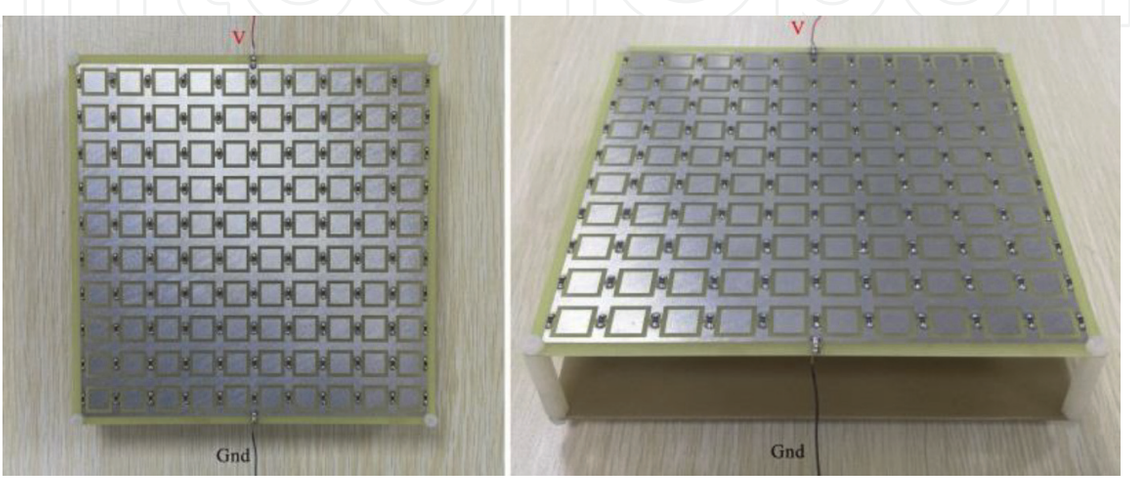

Figure 7.
The photographs of the fabricated antenna.

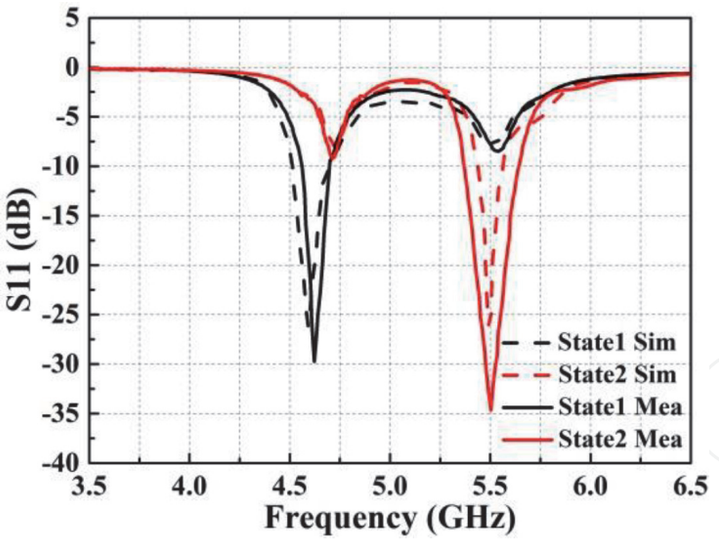

Figure 8.
Simulated and measured S11 of the antenna.

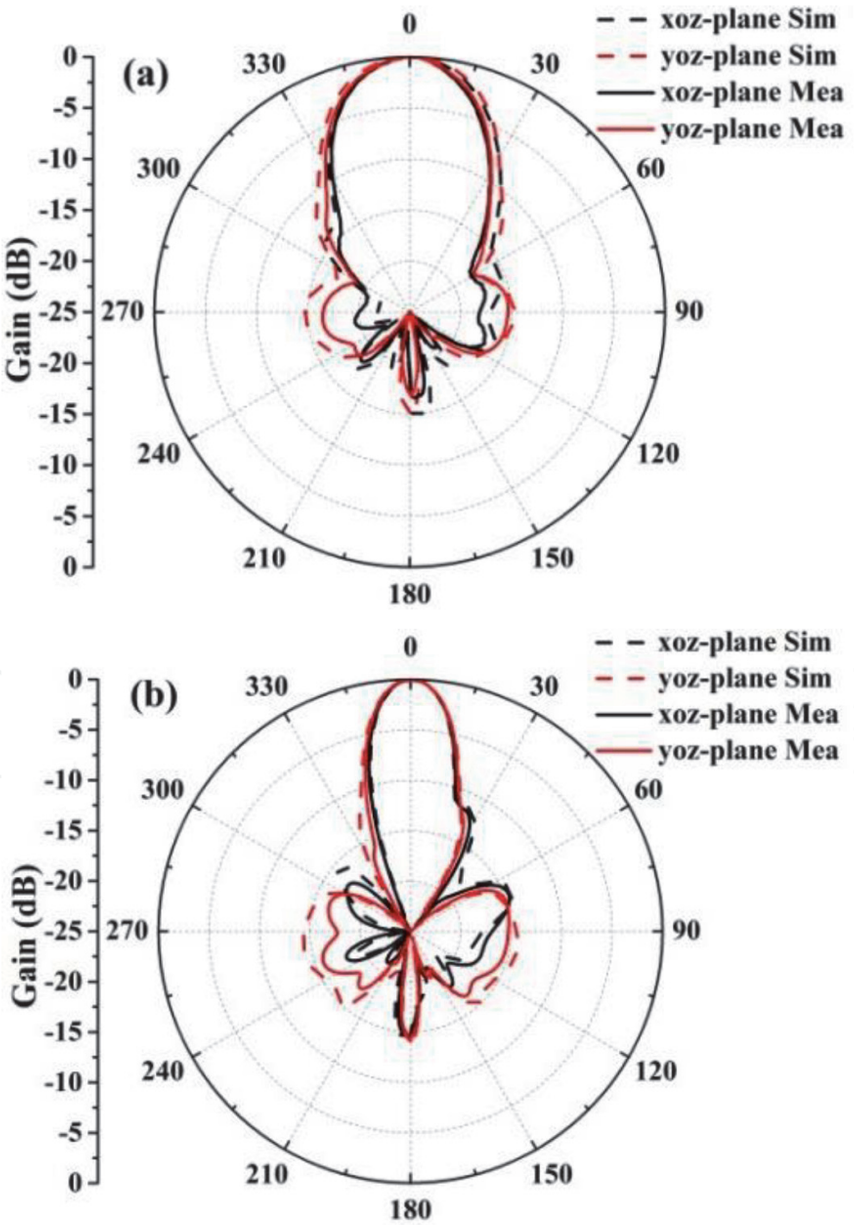

Figure 9.
The radiation patterns of the antenna: (a) 4.6 GHz and (b) 5 GHz.

when f = 4.6 GHz and the diodes are ON, and the red line is the relationship when f = 5.5 GHz and the diodes are OFF. The two lines intersect at the point w = 8 mm and h = 27.2 mm. This indicates that when h = 27.2 mm and w = 8 mm, the antenna can work at 4.6 GHz if the diodes are ON and at 5.5 GHz if the diodes are OFF. So the antenna realizes frequency reconfiguration through tuning the states of the diodes.

3.3 Fabrication and measurement of the antenna

The photographs of the fabricated antenna are shown in **Figure 7**. The red lines connect the anode of the DC source, and the black lines connect the cathode. The S_{11} and radiation patterns of the antenna at two frequencies are measured. Good agreement between the simulated and measured results is obtained. The simulated and measured S11 of the antenna is shown in **Figure 8**. The −10 dB impedance band of the antenna is 4.55–4.7 GHz (3.3%) when diodes are ON and 5.37–5.63 GHz (4.7%) when diodes are OFF. The measured center of the low-frequency band is higher than the simulated result. This may be caused by the fabrication errors. During the welding of SMA joints, some unnecessary metals may be introduced. This results in the deviation of the resonant frequency of the antenna.

Figure 9 presents the simulated and measured radiation patterns of the antenna. **Figure 9a** shows the radiation patterns at 4.6 GHz and **Figure 9b** shows at 5.5 GHz. The measured maximum gain of the antenna is 13.1 dB at 4.6 GHz and 17.1 dB at 5.5 GHz. The 3 dB gain bandwidth of the antenna is 11.9 and 8.2% at two frequency bands, respectively. The gain bandwidth is wider than the impedance bandwidth, so the impedance bandwidth is the working bandwidth of the antenna. The simulated and measured results show that the antenna can realize frequency reconfiguration through tuning the states of the diodes on the PRS. Meanwhile, the antenna obtains well radiation characteristic in both frequencies.

4. Pattern reconfigurable Fabry-Pérot cavity antenna

4.1 Design of the configurable PRS

Firstly, we design a reflection phase reconfigurable unit cell, as shown in **Figure 10**. The unit cell is printed on a substrate of FR4.4 with a thickness of 1.6 mm and permittivity of 4.4. It consists of a square patch and a square ring. A slot is inserted into the unit cell to separate the patch and the ring. Three PIN diodes are

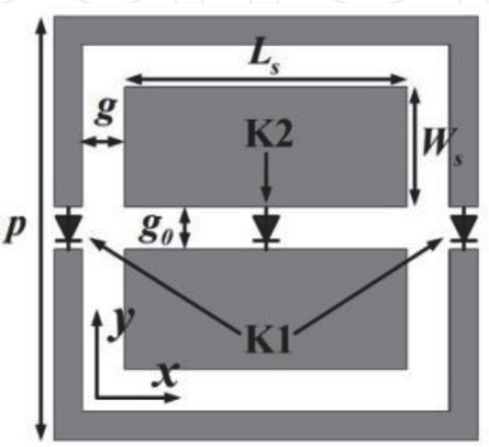

Figure 10.
The structure of the unit cell.

inserted in the slot. The diodes are divided into two groups. The diodes on the ring are named K1 and the diode in the patch is named K2. The different states of two group diodes give the four cell states, as shown in **Table 1**.

The unit cell is simulated by the CST. The simulation setting of the unit cell is the same as the unit cell presented in Section 2. The reflection coefficients of the unit cell under *y*-polarized wave are shown in **Figure 11**. The simulation results show that the reflection phase of the unit cell at 5 GHz ranged from −165 to −262°. This suggests that the unit cell has a large range of reflection phase variation. Meanwhile, the reflection magnitudes of the unit cell in four states are always greater than 0.7. This can ensure a high gain of the FPC antenna.

A reconfigurable PRS is formed by the unit cell shown in **Figure 10**. The structure of the PRS is shown in **Figure 12**. It is composed by 6 × 6 unit cells and divided

Diodes	S1	S2	S3	S4
K1	OFF	OFF	ON	ON
K2	OFF	ON	OFF	ON

Table 1.
The four states of the unit cell.

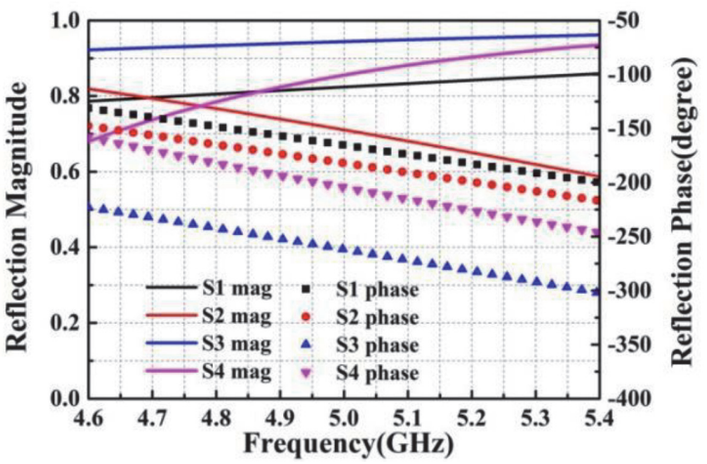

Figure 11.
The reflection phase of the unit cell.

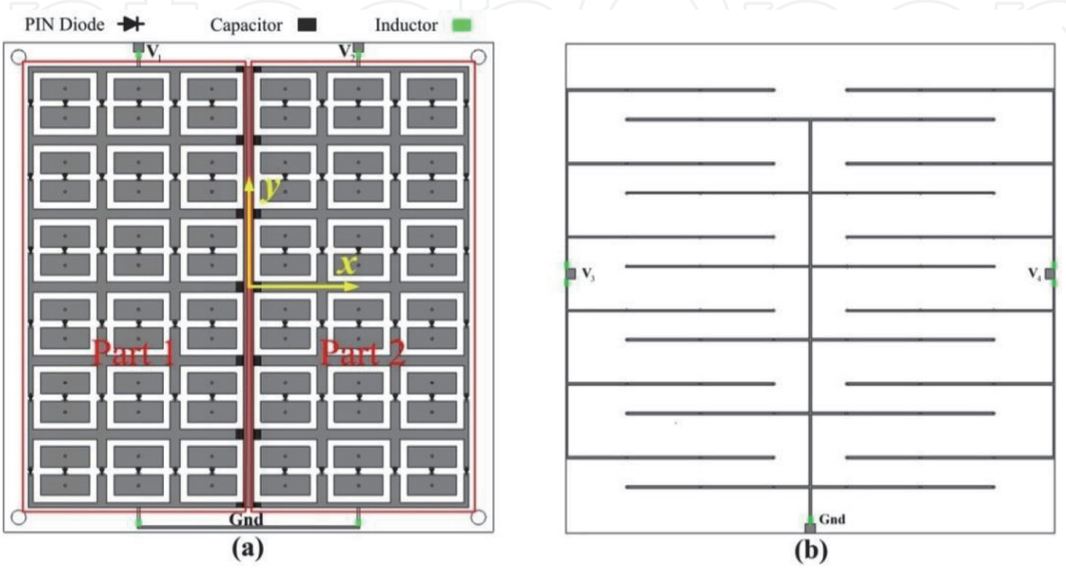

Figure 12.
The structure of the PRS: (a) top view and (b) bottom view.

into two parts. The reflection phase of two parts of the PRS can be controlled by tuning the states of the PIN diodes. Some DC-biased circuit is added on the PRS to bias the PIN diodes. Firstly, since the square rings in the unit cells form a net structure when combing the PRS and the K1 is on the net structure, so two lines of capacitors (220 pF) are added between the two parts to bias the K1 in different parts of the PRS independently. In **Figure 12a**, the points V1 and V2 are used to bias the K1 in different parts. Then, in order to bias the K2, two metalized via hole are added into each unit cell to connect two parts of the patch, and the biasing lines on the bottom side of the PRS which are shown in **Figure 12b**. The points V3 and V4 are used to bias the K2 in different parts of the PRS. The Gnd on the top and bottom side of the PRS are connected by a metalized via hole. Some inductors (20 nH) are inserted into the lines to prevent the RF signal from going into the DC sources. With the designed biasing lines, the K1 and K2 in different parts of the PRS can be controlled independently. The biasing lines are very thin (0.2 mm), and the diameter of the metalized via holes is tiny enough (0.3 mm). So the simulated results show that the DC biasing circuits have barely influence on the performance of the metasurface.

4.2 Antenna design

From the theoretical analysis in Section 1, when the PRS has a uniform reflection phase, the antenna radiates toward the broadside direction [16]. And the main beam of the antenna is perpendicular to the antenna surface. However, when the PRS have reflection phase gradient, the main beam of the antenna will be tilted. So when the two parts of the PRS have different reflection phases, the beam of the antenna will tilt to the direction that has lagging phase.

The structure of the FPC antenna is shown in **Figure 12**, and the values of the parameters of the antenna are shown in **Table 2**. The FPC antenna is feed by a slot coupled patch antenna, as shown in **Figure 13a**. The feed antenna is set under the PRS with a distance of h. The side view of the FPC antenna is shown in **Figure 13b**.

p	Ls	Ws	g	g_0	Lp	L	h
15	10	4.25	1.5	1.5	10.4	100	30.5

Table 2.
Values of the parameters (mm).

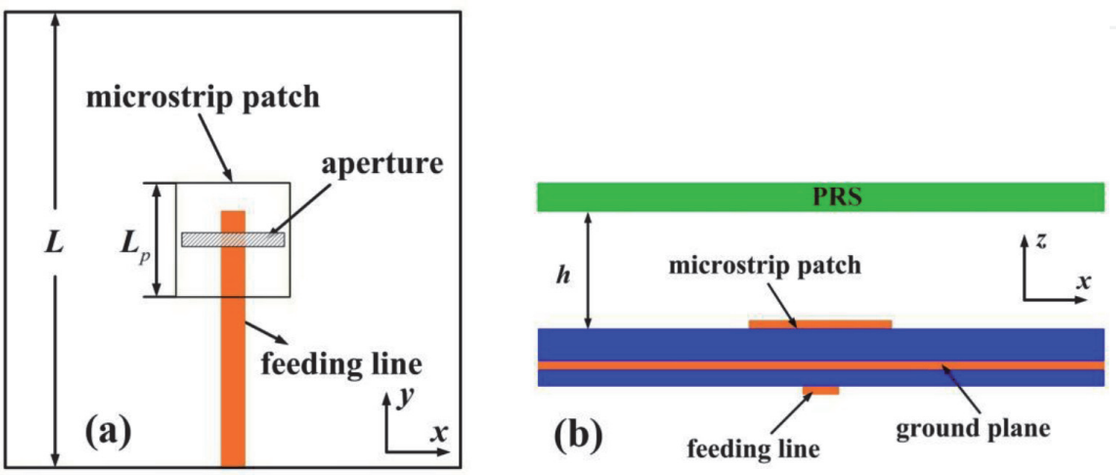

Figure 13.
Structure of the antenna: (a) top view of the feeding antenna and (b) side view of the FPC antenna.

Through controlling the states of the diodes, the PRS will present different reflection phase distributions, so the beam of the antenna will tilt toward different directions. Due to the large reflection phase variation range, the antenna obtains a large steering angle. The antenna operates at 5 GHz and the reflection phase gradient of the PRS is along *x*- direction, so the beam of the antenna will tilt in *xoz* plane. We calculate the height of the cavity when the PRS is in the state of S1. After being optimized by the CST, the *h* is set to 30.5 mm finally.

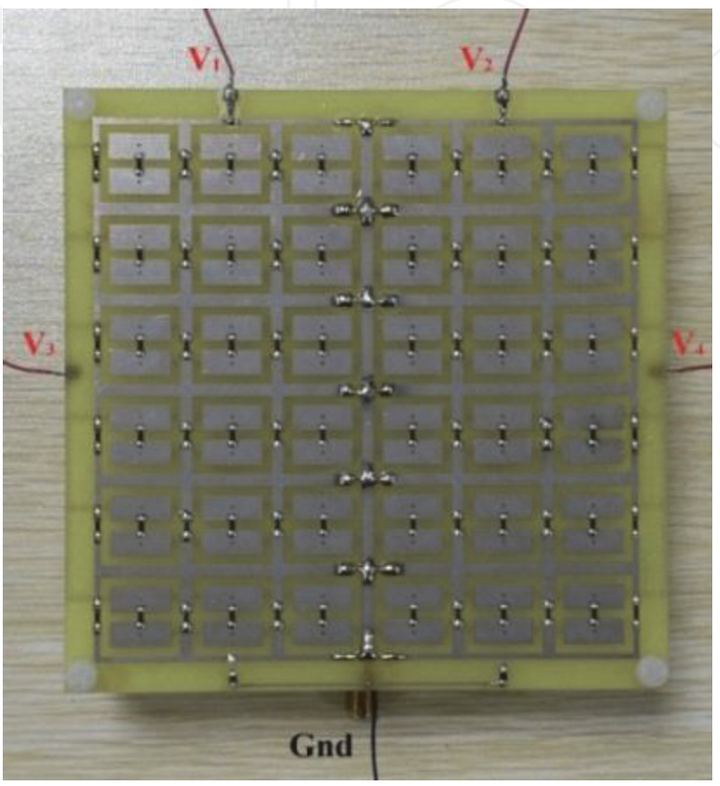

Figure 14.
Photograph of the fabricated antenna.

States	Part 1		Part 2		Beam direction (°)	Gain (dB)
	K1	K2	K1	K2		
1	OFF	OFF	OFF	OFF	0	11.1
2	OFF	ON	OFF	OFF	−6	9.8
3	OFF	OFF	OFF	ON	6	9.8
4	ON	ON	OFF	OFF	−18	8.7
5	OFF	OFF	ON	ON	18	8.7
6	ON	OFF	ON	ON	−24	7.6
7	ON	ON	ON	OFF	24	7.6
8	ON	OFF	OFF	ON	−46	6.6
9	OFF	ON	ON	OFF	46	6.6
10	ON	OFF	OFF	OFF	−54	6.3
11	OFF	OFF	ON	OFF	54	6.3

Table 3.
Detail information of the antenna at different states.

4.3 Fabrication and measurement of the antenna

The photograph of the fabricated antenna is shown in **Figure 14**. After simulation, we find that the antenna can work in at kinds of states. We measured the S_{11} and radiation patterns of the antenna in these 11 states. **Table 3** gives the detail performance of the antenna in different states, including the states of the diodes, beam directions, and maximum gain. Because the antenna structure at state 2 (4, 6, 8, 10) is completely symmetrical to that at state 3 (5, 7, 9, 11), so they have same the S_{11}. For simplicity, we just show the simulated and measured S11 in states of 1, 2, 4, 6, 8, and 10 in **Figure 15**. The measured results agree well with the simulated ones. The measured impedance bandwidth of the antenna is 4.92–5.08 GHz (3.2%). The S_{11} of the antenna only has little difference between different states.

The radiation patterns of the antenna are measured in anechoic chamber. The simulated and measured radiation patterns of the antenna are presented in **Figure 16**. Good agreement is obtained between the measured results and the simulated ones. We know that the main beam of the antenna tilts in *xoz* plane,

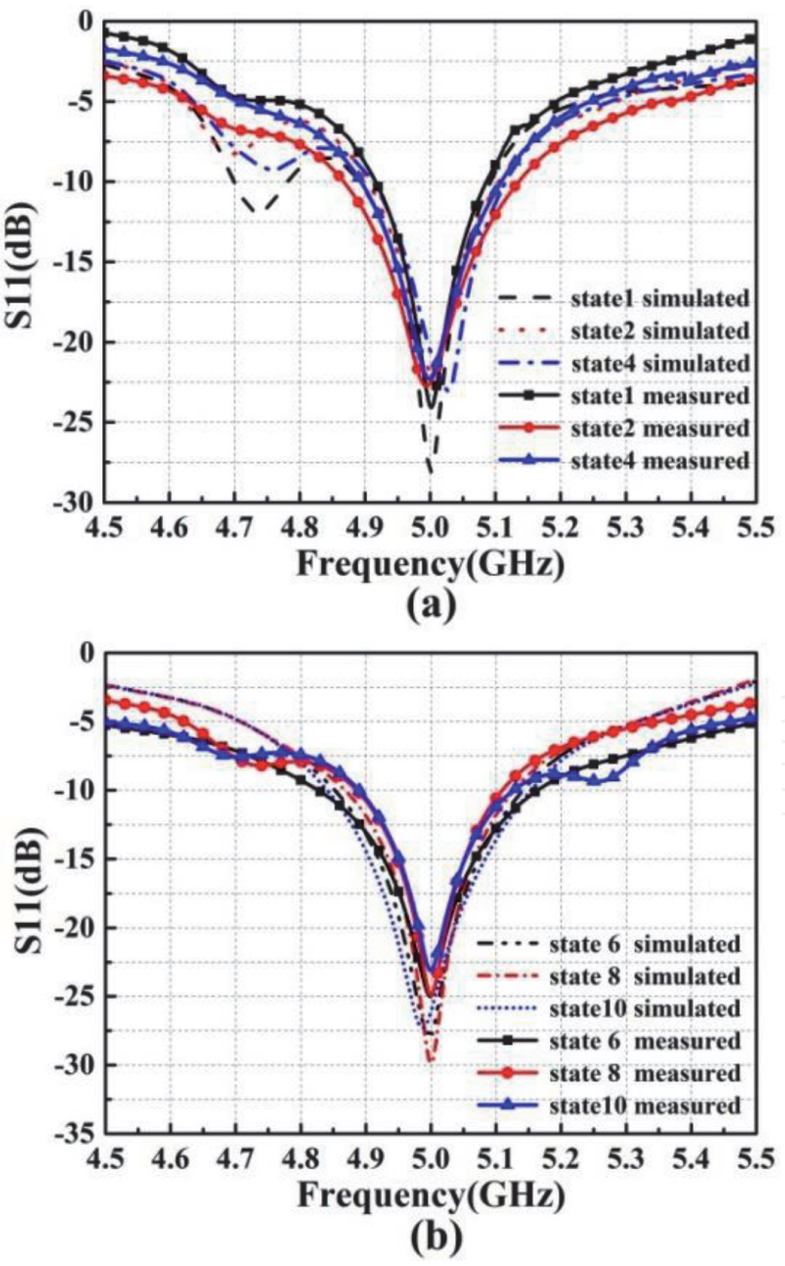

Figure 15.
Simulated and measured S11: (a) states 1, 2, and 4 and (b) states 6, 8, and 10.

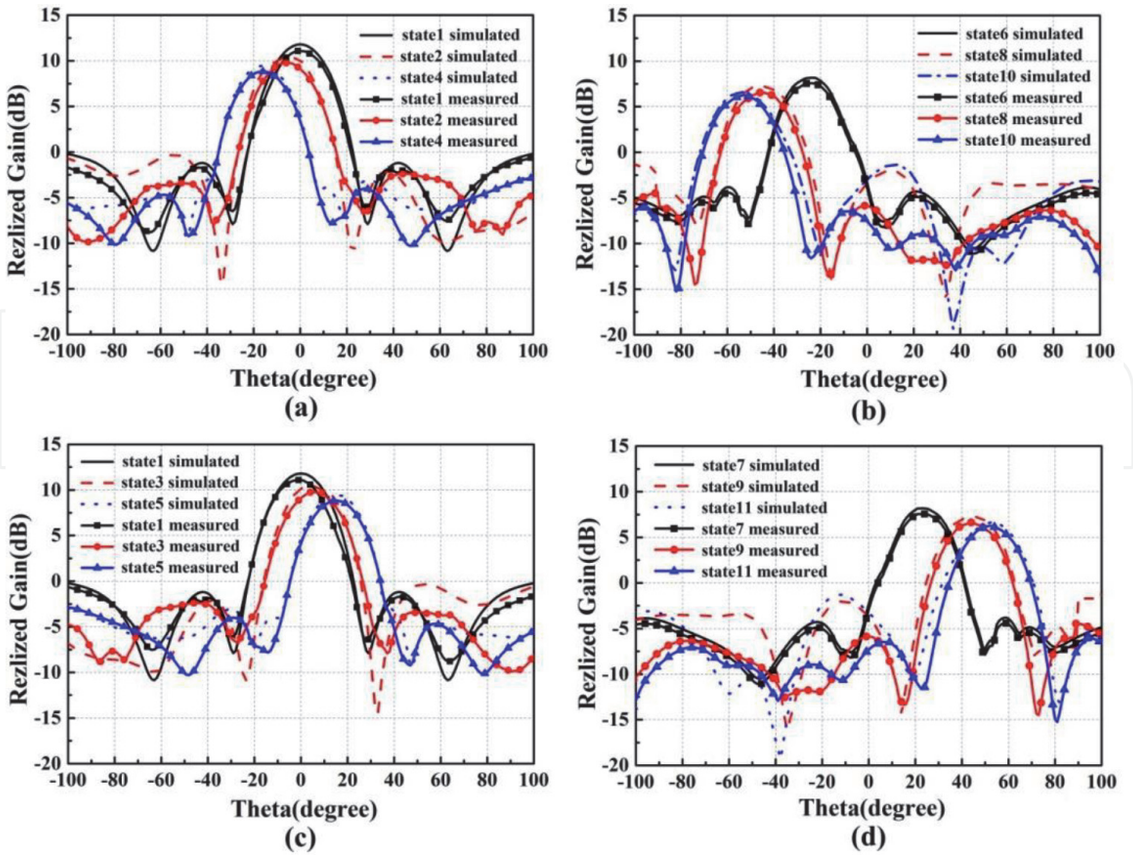

Figure 16.
Radiation patterns of the antenna: (a) states 1, 2, and 4; (b) states 6, 8, and 10; (c) states 1, 3, and 5; and (d) states 7, 9, and 11.

so the radiation patterns of the antennas are all in *xoz* plane. The main beam of the antenna in state 1 is toward the *+z* direction. However, it tilts to *–y* direction in states 2, 4, 6, 8, and 10 and to *+y* direction in states 3, 5, 7, 9, and 11. And the same tilted angle is obtained at states 2 (4, 6, 8, 10) and 3 (5, 7, 9, 11).

The simulated maximum gain of the antenna at state 1 is 11.8 dB, and the measured maximum gain is 11.1 dB. With the increase of the beam tilted angle, the maximum gain of the antenna decreases. The antenna obtains maximum beam tilted angle (about 54°) at states 10 and 11, and the maximum gain of the antenna decreases to 6.3 dB. The antenna remains to have high-gain performance while realizing beam tilting. Besides, the gain floating of the antenna at all states in the operating band are less than 2.8%. So the impedance bandwidth of the antenna is the working band of the antenna.

5. Polarization and pattern reconfigurable FPC antenna

5.1 Design of the reconfigurable PRS

In the last section, we design an FPC antenna with large beam steering angle. However, it can only realize beam tilting in one plane. In practice application, we prefer the antenna to be able to steer the beam in two directions. So in this Section, we will design a configurable PRS to realize two-dimensional beam steering of the FPC antenna [17].

The unit cell of the PRS is shown in **Figure 17**. It is also printed on the substrate of FR4. Each unit cell consists of four square patches. Four PIN diodes are inserted between two adjacent patches. The four diodes are controlled simultaneously, and the

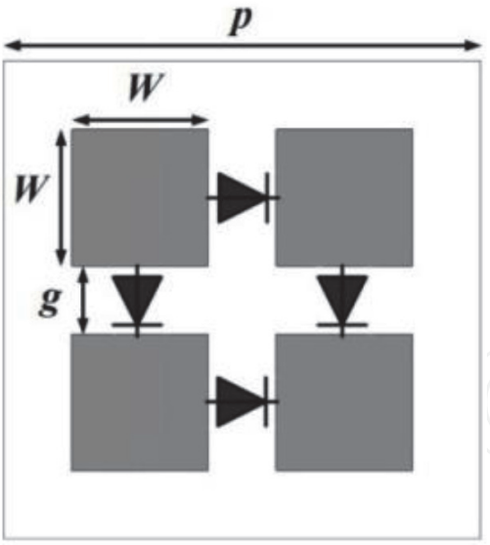

Figure 17.
The unit cell of the PRS.

unit cell can present two states. The unit cell has different reflection coefficients in different states. The reflection coefficients of the unit cell are simulated by the CST, and the results are shown in **Figure 18**. We can see that the unit cell has the same reflection coefficients for both polarization waves. The reflection phases of the unit cell in two states at 5.5 GHz are −187° and −217°, respectively. And the reflection magnitude is always larger than 0.75. This suggests that the unit cell remains to have high reflectivity when tuning the reflection phase through controlling the state of the diodes. The high reflectivity ensures the high gain of the antenna.

We compose a PRS with 6 × 6 unit cells by the unit cell shown in **Figure 17**. The top view of the PRS is shown in **Figure 19**. The PRS is divided into four parts. The diodes in different parts can be controlled independently. Through tuning the state of the diodes in different parts, the PRS presents different reflection phase distributions. A DC biasing circuit is designed on the PRS to realize independent control of the diodes in different parts. Two patches of each unit cell are connected to the biasing lines on the bottom side of the PRS through metalized via holes. By reasonably arranging the orientation of the diodes in each unit cell, the diodes can be controlled simultaneously. The biasing lines on the bottom of the PRS are shown in **Figure 20b**. The biasing point V1, V2, V3, and V4 are connected to the anode of the

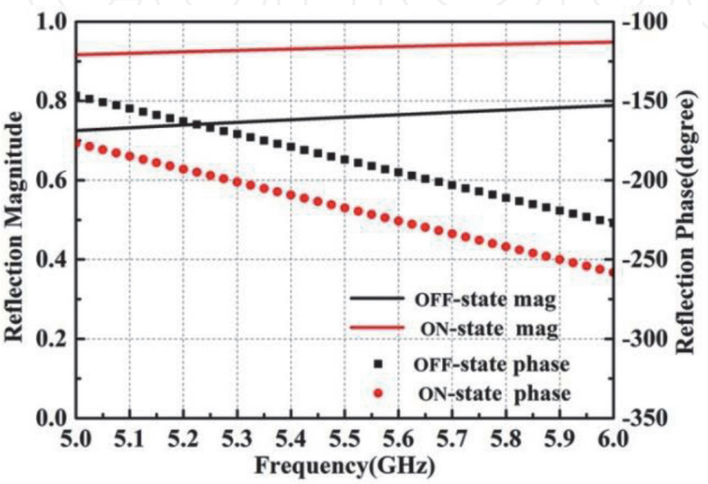

Figure 18.
The reflection coefficients of the unit cell.

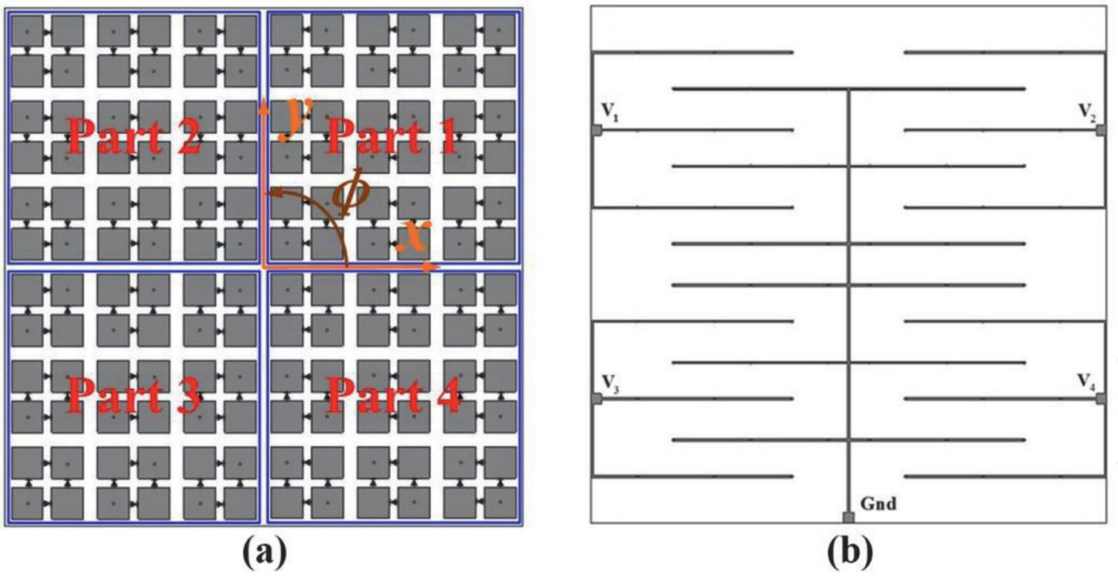

Figure 19.
The structure of the PRS: (a) top view and (b) bottom view.

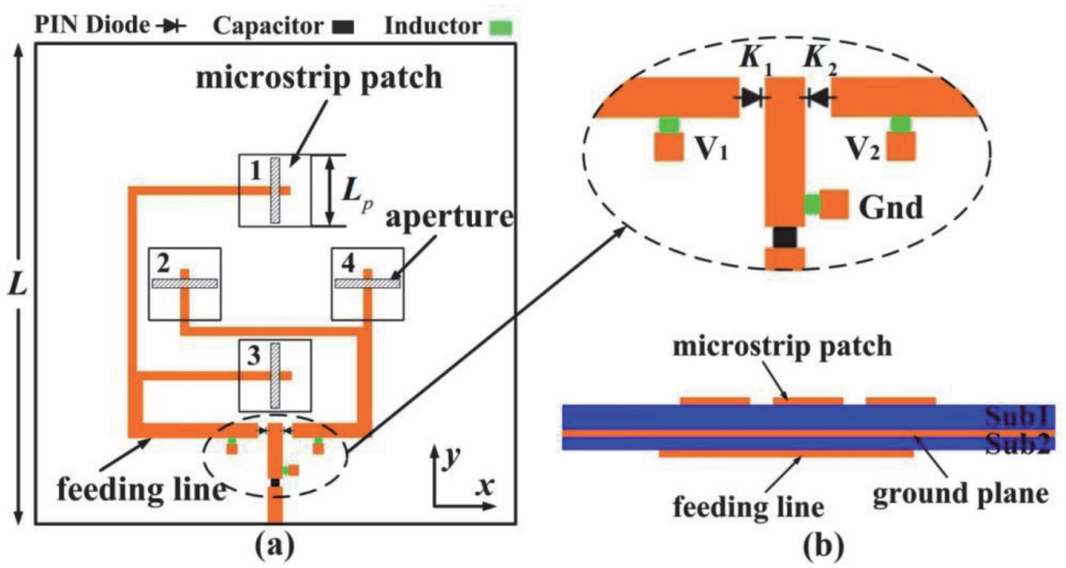

Figure 20.
Polarization configurable feeder antenna: (a) top view and (b) side view.

DC source, and the Gnd is connected to the cathode. The width of the biasing line is 0.2 mm, and the diameter of the metalized via holes is 0.3 mm to reduce the influence of biasing lines on the RF signal.

5.2 Design of the polarization configurable feeder antenna

In order to realize the polarization configuration of the antenna, a polarization configurable feeder antenna is needed. So we designed a polarization configurable slot coupled patch antenna, as shown in **Figure 20**. The feeder antenna is composed by two substrates with different thickness (1.6 mm for Sub1 and 0.8 mm for Sub2). Four identical patches are chosen as the radiators of the antenna. They are printed on the top side of the Sub1 and are symmetric with respect to the center of the antenna. Between the two substrates is a metal ground plane, and four slots are etched on the plane under four patches. The slots 1 and 3 are along the y direction, and the slots 2 and 4 are along the x direction. The feeding line is printed on the bottom side of the Sub2. The four stubs are used to feed four patches through slots.

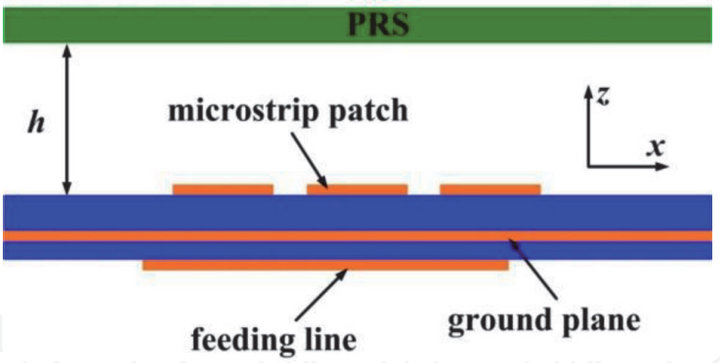

Figure 21.
Geometry of the FPC antenna.

States	Part 1	Part 2	Part 3	Part 4	Beam direction
1	OFF	OFF	OFF	OFF	Broadside
2	ON	OFF	OFF	ON	φ = 0°
3	ON	OFF	OFF	OFF	φ = 45°
4	ON	ON	OFF	OFF	φ = 90°
5	OFF	ON	OFF	OFF	φ = 135°
6	OFF	ON	ON	OFF	φ = 180°
7	OFF	OFF	ON	OFF	φ = 225°
8	OFF	OFF	ON	ON	φ = 270°
9	OFF	OFF	OFF	ON	φ = 315°

Table 4.
Detail information of the antenna at different states.

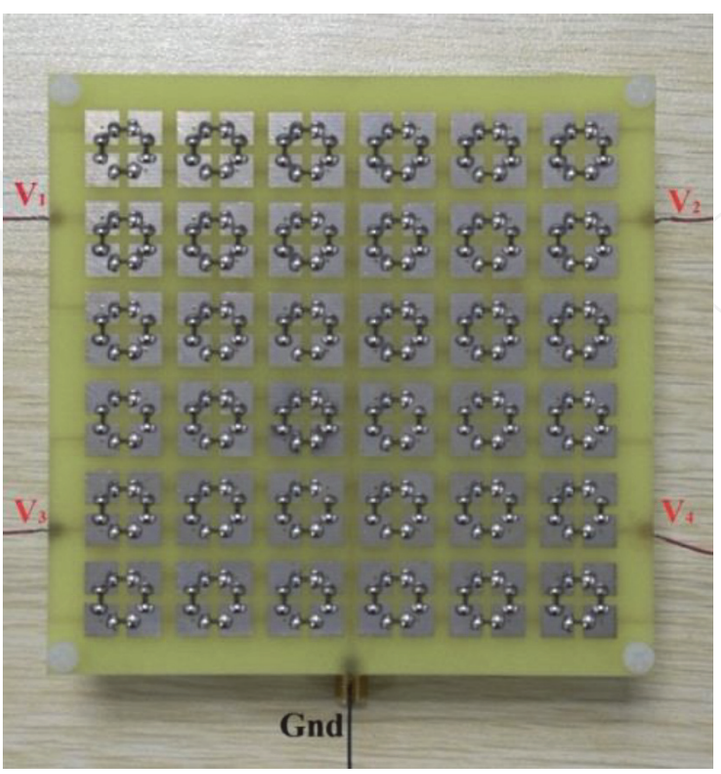

Figure 22.
The photograph of the fabricated antenna.

The lengths of the four stubs are properly designed to make the patches receive the excited with the same phase. Two PIN diodes K1 and K2 are inserted into the feeding line. The biasing points V1, V2, and Gnd are added near the microstrip line to bias the PIN diodes. These points are connected to the microstrip line through inductors. The inductors can allow DC to pass through and block the RF signals. When V1 connects the anode of the DC source, the K1 is turned ON, and when V2 connects the anode of the DC source, the K2 is turned ON. When K1 is ON and K2 is OFF, patches 1 and 3 are excited and the antenna radiates *x*-polarized wave. Whereas when K1 is OFF and K2 is ON, patches 2 and 4 are excited and the antenna radiates *y*-polarized wave. Besides, in order to prevent the DC from going into the RF sources, a slot is added in the microstrip line, and a capacitor is inserted into the slot. The capacitor can allow RF signal to pass through and block the DC.

5.3 Design of the antenna

Using the proposed configurable PRS and the polarization configurable patch antenna, a polarization and pattern reconfigurable FPC antenna are formed, as shown in **Figure 21**. The PRS is set above the feeder antenna with a distance of h. The antenna is designed to work at 5 GHz. The height of the cavity h is calculated

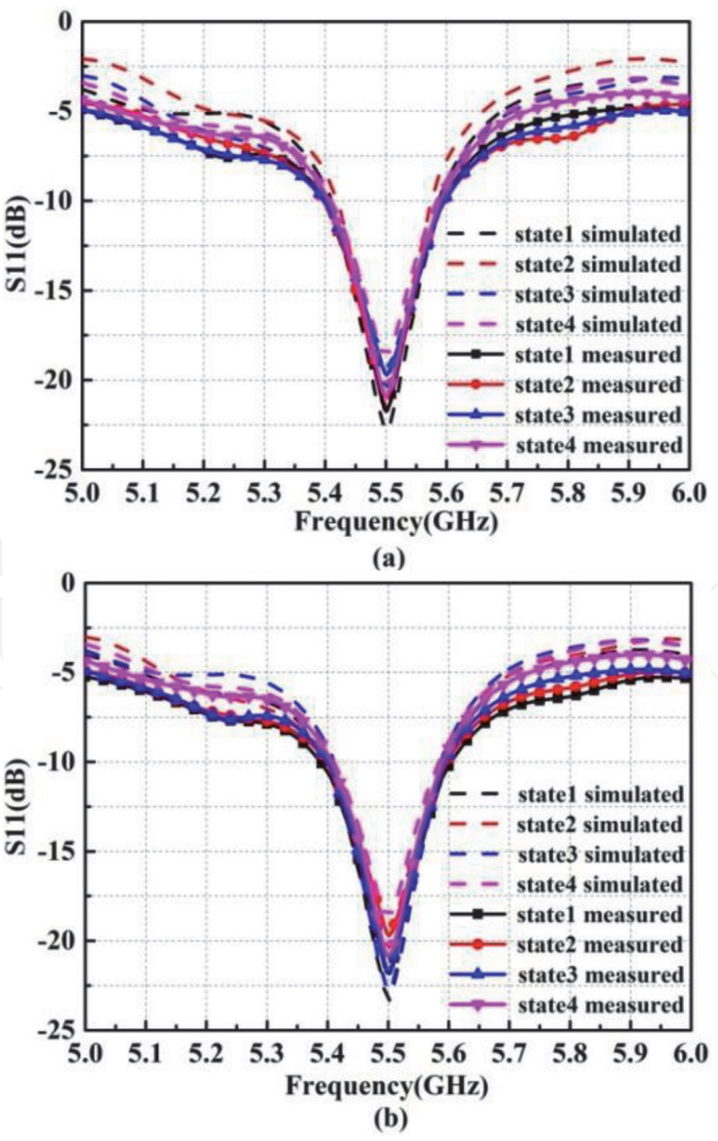

Figure 23.
Simulated and measured S11 of the antenna: (a) x-polarized and (b) y-polarized.

according to Eq. (9) with the reflection phase of the unit cell when diodes are OFF. After being optimized, the h is set to 28 mm.

Through controlling the diodes in four parts of the PRS, the PRS can present nine different states, and the antenna obtains nine beam directions in both polarizations. **Table 4** gives the detailed information of the antenna at different states. Due to the PRS having the same function on different polarized waves, the antenna has the same beam direction at the same diode states for different polarizations.

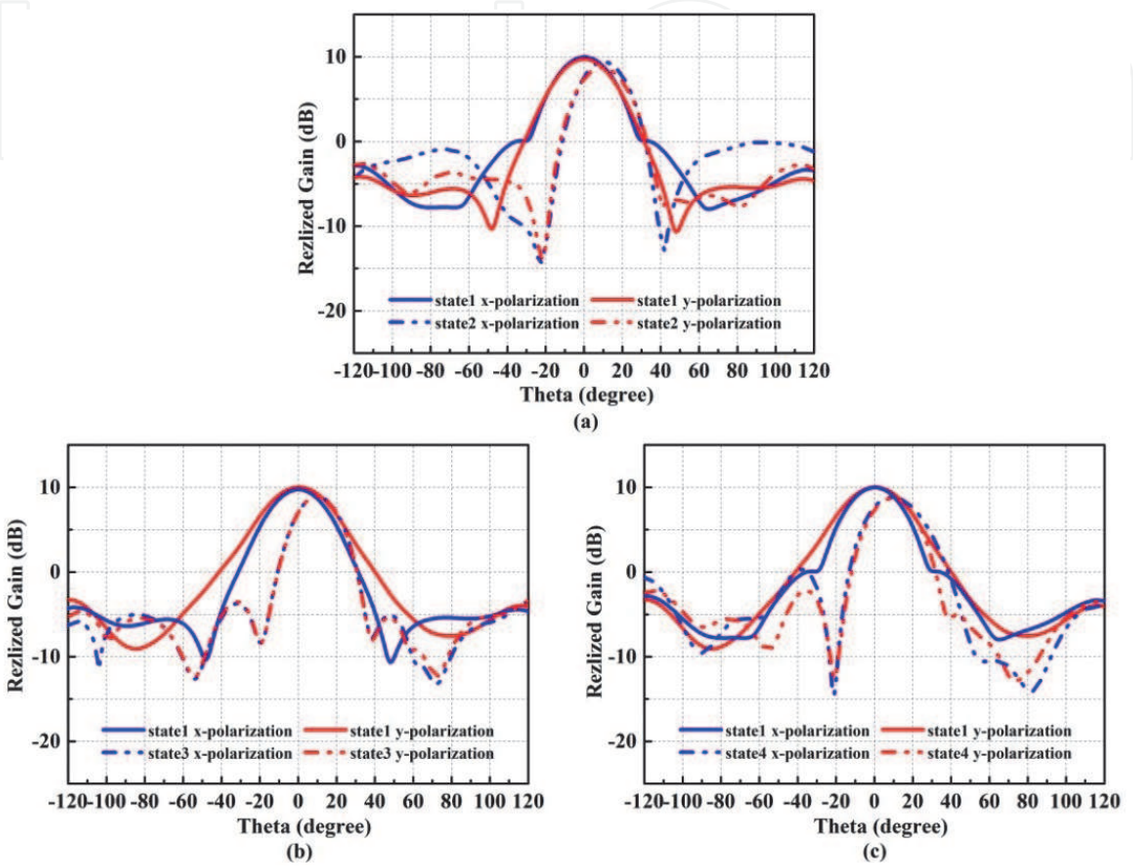

Figure 24.
The radiation patterns of the antenna: (a) φ = 0°, (b) φ = 45°, and (c) φ = 90°.

States	Beam tilted angle (°)	Gain (dB)	Direction (dBi)	Aperture efficiency (%)	Radiation efficiency (%)
1	0	9.7	12.5	27.3	52.5
2	10	8.7	12	21.7	46.8
3	8	8.9	11.9	22.7	50.1
4	10	8.7	12	21.7	46.8
5	8	8.9	11.9	22.7	50.1
6	10	8.7	12	21.7	46.8
7	8	8.9	11.9	22.7	50.1
8	10	8.7	12	21.7	46.8
9	8	8.9	11.9	22.7	50.1

Table 5.
The antenna performance.

5.4 Fabrication and measurement of the antenna

Figure 22 shows the photograph of the fabricated antenna. We measured the reflection coefficients and the radiation patterns of the antenna. Because of the symmetry of the PRS, the simulated and measured results of the antenna in states 2 and 6 (states 4 and 8 and states 3, 5, 7, and 9) are almost the same. So we just show the results in states 1, 2, 3, and 4.

Figure 23 plots the simulated and measured S_{11} of the antenna at states 1, 2, 3, and 4. **Figure 23a** is the result under x- polarization and **Figure 23b** is under y-polarization. The measured impedance bandwidth of the antenna is 5.4–5.6 GHz (3.6%). Because the feeder of the antenna remains constant in different states, the S_{11} of the antenna in different states varies very little. The measured results agree well with the simulated ones.

The radiation patterns of the antenna are measured in anechoic chamber. **Figure 24** plots the measured results of the antenna. **Figure 24a** is the radiation pattern of the antenna at states 1 and 3 in the plane of φ = 0°, **Figure 24b** is at states 1 and 3 in the plane of φ = 45°, and **Figure 24c** is at states 1 and 4 in the plane of φ = 90°. The results show that the main beam of the antenna is in the $+z$ direction at state 1 and tilts in the plane of φ = 0°, φ = 45°, and φ = 90° at states 2, 3, and 4, respectively. The tilted angle at states 2 and 4 is 10° and that at state 3 is 8°. The maximum gains of the antenna at different states are also measured. The antenna achieves maximum gain of 9.7 dB at state 1, 8.9 dB at state 3, and 8.7 dB at states 2 and 4. Meanwhile, the antenna obtains stable gain at all states. The gain floating of the antenna at all states are less than 2.3% within the impedance bandwidth. **Table 5** summarizes the antenna performance. The beam tilted angle and gain are measured results and the directivity is simulated results. The aperture efficiency is calculated by the gain and size of the antenna, as shown in Eq. (12). And the radiation efficiency is calculated by the gain and direction, as shown in Eq. (13).

$$\eta_1 = G\frac{{\lambda_0}^2}{4\pi A} \tag{12}$$

$$\eta_2 = G/D \tag{13}$$

6. Conclusion

In this chapter, we summarize our recent efforts in realizing reconfigurable FPC antenna basing on the reconfigurable MS. PIN diodes are added on the MS to realize the reflection phase control. Using the flexible phase control capability of the MS, it is easy to tune the frequency and radiation pattern of the FPC antenna, so as to realize reconfigurable FP antenna. The reconfigurable FPC antenna is a good way to improve the performance of antenna. This method can make the FPC antenna more widely used in the field of wireless communication systems.

Abbreviations

FP	Fabry-Pérot
FPC	Fabry-Pérot cavity
MS	metasurface
PRS	partially reflection surfaces

Author details

Peng Xie, Guangming Wang*, Haipeng Li, Yawei Wang and Xiangjun Gao
Air Force Engineering University, Air and Missile Defense College, Xi'an, Shaanxi Province, China

*Address all correspondence to: wgming01@sina.com

References

[1] Trentini GV. Partially reflecting sheet arrays. IRE Transactions on Antennas and Propagation. 1956;**4**(4): 666-671

[2] Zeb BA, Hashmi RM, Esselle KP, Ge Y. The use of reflection and transmission models to design wideband and dual-band Fabry-Perot cavity antennas. In: 2013 International Symposium on Electromagnetic Theory; 2013. pp. 1084-1087

[3] Abdelghani ML, Attia H, Denidni TA. Dual- and wideband Fabry–Perot resonator antenna for WLAN applications. IEEE Antennas and Wireless Propagation Letters. 2017;**16**: 473-476

[4] Kim D, Jeongho J, Choi J. A broadband Fabry-Perot cavity antenna designed using an improved resonance prediction method. Microwave and Optical Technology Letters. 2011;**53**(5): 1065-1069

[5] Wang N, Liu Q, Wu C, Talbi L, Zeng Q, Xu J. Wideband Fabry-Perot resonator antenna with two complementary FSS layers. IEEE Transactions on Antennas and Propagation. 2014;**62**(5):2463-2471

[6] Konstantinidis K, Feresidis AP, Hall PS. Multilayer partially reflective surfaces for broadband Fabry-Perot cavity antennas. IEEE Transactions on Antennas and Propagation. 2014;**62**(7): 3474-3481

[7] Kim D. Noval dual-band Fabry-Pérot cavity antenna with low frequency separation ratio. Microwave and Optical Technology Letters. 2009;**51**(8): 1869-1872

[8] Meng F, Sharma SK. A dual-band high-gain resonant cavity antenna with a single layer superstrate. IEEE Transactions on Antennas and Propagation. 2015;**63**(5):2320-2325

[9] Debogović T et al. Dual-polarized partially reflective surface antenna with MEMS-based beamwidth reconfiguration. IEEE Transactions on Antennas and Propagation. 2014;**62**(1): 228-236

[10] Sultan F, Mitu SSI. Superstrate-based beam scanning of a Fabry–Perot cavity antenna. IEEE Antennas and Wireless Propagation Letters. 2016;**15**: 1187-1190

[11] Guzmán-Quirós R, Weily AR, Gómez-Tornero JL, Guo YJ. A Fabry–Pérot antenna with two-dimensional electronic beam scanning. IEEE Transactions on Antennas and Propagation. 2016;**64**(4):1536-1541

[12] Ji LY, Guo YJ, Qin PY, Gong SX, Mittra R. A reconfigurable partially reflective surface (PRS) antenna for beam steering. IEEE Transactions on Antennas and Propagation. 2015;**63**: 2387-2395

[13] Guzmán-Quirós R, Gómez-Tornero JL, Weily AR, Guo YJ. Electronically steerable 1-D Fabry-Perot leaky-wave antenna employing a tunable high impedance surface. IEEE Transactions on Antennas and Propagation. 2012;**60**: 5046-5055

[14] Ourir A et al. Directive metamaterial-based subwavelength resonant cavity antennas—Applications for beam steering. Comptes Rendus Physique. 2009;**10**(5):415-422

[15] Xie P, Wang G. Design of a frequency reconfigurable Fabry-Pérot cavity antenna with single layer partially reflecting surface. Progress in Electromagnetics Research. 2017;**70**: 115-121

[16] Xie P, Wang G, Cai T, Li H, Liang J. A dual-polarized two-dimensional beam-steering Febry-Pérot cavity antenna with a reconfigurable partially reflecting surface. IEEE Antennas and Wireless Propagation Letters. 2017;**16**: 2370-2374

[17] Xie P, Wang G, Cai T, Li H, Liang J. Novel Fabry-Pérot cavity antenna with enhanced beam steering property using reconfigurable meta-surface. Applied Physics A: Materials Science and Processing. 2017;**123**(7):462